



Effect of temperature and strain rate on the hot workability behaviour of Ni–25Cr–14W superalloy: An approach using processing map and constitutive equation

Ravi Ranjan Kumar^{1,a)} , Randhir Kumar Singh², Varsha Florist¹, Namit Pai³, C. R. Anoop¹, Debasis Tripathy¹, S. V. S. Narayana Murty¹

¹ Liquid Propulsion Systems Centre, Thiruvananthapuram 695547, India

² Malaviya National Institute of Technology Jaipur, Jaipur 302017, India

³ Indian Institute of Technology Bombay, Mumbai 400076, India

^{a)} Address all correspondence to this author. e-mail: raviranjana.dei@gmail.com

Received: 11 January 2024; accepted: 2 July 2024; published online: 22 July 2024

The hot workability of Ni–25Cr–14W alloy is studied through isothermal hot compression tests in the temperature (T) range of 1000–1200 °C and in the strain rates ($\dot{\epsilon}$) of 0.001–10 s⁻¹ in a thermomechanical simulator. Flow stress data show stable flow curves at T > 1050 °C and $\dot{\epsilon}$ < 0.1 s⁻¹. The values of flow stress decrease with increase in T or decrease in $\dot{\epsilon}$. Based on processing map, safe region for hot workability has been identified in the temperature range of 1000–1200 °C and $\dot{\epsilon}$ of 0.001–0.1 s⁻¹ with maximum efficiency (η) of ~44% at 1175 °C and 0.001 s⁻¹. Dynamic recrystallization has been identified as the softening mechanism operating in the material at high temperature and lower $\dot{\epsilon}$. Incomplete recrystallization of the microstructures was noted during multi-step forging by varying T or $\dot{\epsilon}$, indicating the importance of maintaining the same during industrial processing.

Introduction

Nickel-based superalloys are workhorse materials for high-temperature applications, exhibiting good strength, oxidation resistance, creep and stress-rupture property at high temperatures, as high as 0.8 T_m (T_m is melting temperature in Kelvin) [1]. These alloys have wide range of applications from cryogenic to high temperatures due to their FCC phase stability. Nickel-based alloys have critical applications in high-temperature sections of supercritical power plants [2–7], gas turbines [2, 7–9] blades, disc cases, jet engine components, rocket engine parts [10–12] such as combustor nozzles, turbines rotors, discs, casings, chemical process industries, and in other specialized applications requiring heat and/or corrosion resistance [5, 6, 13, 14]. In today's scenario, nickel-based superalloys constitute over 40–50% of the weight of advanced aircraft engines.

Ni–Cr–W alloy is a relatively new family of solid solution strengthened nickel-based superalloys, containing alloying elements such as Cr, W, Mo and Ta having high melting point and low diffusivities. These elements further promote formation

of primary MC type carbides or secondary carbides M₆C and M₂₃C₆ during heat treatment [15]. These alloys have excellent high-temperature mechanical strength and long-term creep rupture strength up to 1000 °C [16, 17]. The potential applications of this alloy are in aerospace and chemical process industries for gas turbine hot sections, combustion sections, heat exchanger tubes and industrial furnace fixtures [17, 18]. In this Ni–Cr–W alloy family, some of prominent alloys are Haynes 230, Ni–19Cr–21.5W and GH3128. The Haynes 230 alloy additionally contains Mo, Al for high-temperature oxidation resistance, La and B for improving hot corrosion resistance and rupture ductility, respectively [19]. Ni–25Cr–14W is another superalloy in this family containing small amount of Ti, Al, Fe and C, which is equivalent to Russian grade XH60BT.

The nickel-based alloys are realised through ingot metallurgical processing involving vacuum induction melting followed by thermomechanical processing. During wrought product realisation, premium vacuum melted cast ingot undergoes various thermomechanical processes to realise the desired products in

the form of rods, forged blocks and sheets. However, the hot working of nickel-based superalloys is very challenging, because of their high strength at elevated temperatures ($> 900\text{ }^{\circ}\text{C}$) and as these are heavily alloyed with multiple alloying elements to their saturation levels. These factors lead to increased susceptibility for microstructure instability, segregation of alloying elements and formation of cracks during hot working operations. The microstructure evolution of material during hot deformation is dynamic in nature and is controlled by the balance of work hardening and flow softening caused by dynamic recovery and dynamic recrystallization [20]. Therefore, it is essential to have optimum hot working parameters (strain, strain rate and temperature) to achieve desired homogeneous microstructure, grain size and isotropic mechanical properties [21–23].

In recent years, hot deformation testing was successfully employed to generate processing map based on dynamic material model [16, 20, 22, 24, 25] and identify the ‘safe’ processing conditions through instability criterion proposed by various researchers [24, 26, 27]. The processing map provides information on safe windows of temperature (T), strain rate ($\dot{\epsilon}$) and strain (ϵ), which will yield optimum combination of microstructure, grain size and mechanical properties in the material. This further provides the information about unstable parameters (T , $\dot{\epsilon}$ and ϵ), which should be avoided during hot working. The flow curves (true stress–true strain) obtained from hot compression test are analysed mathematically along with hot deformation parameters (apparent activation energy, strain rate sensitivity) to develop the processing maps [22, 24, 25] and constitutive equations [28, 29]. The constitutive equation is used to predict the flow stress/load and energy consumption requirement, before actual deformation to plan the establishment of hot working facility suitably.

Liu et al. [16] have studied the hot deformation behaviour of the as-cast Ni–Cr–W alloy (Haynes 230 alloy) and identified the maximum peak efficiency of $\sim 44\%$ on the sample deformed at $1200\text{ }^{\circ}\text{C}$ under slow strain rate of 0.001 s^{-1} and softening mechanism for microstructural evolution was identified as dynamic recrystallization (DRX). It is further reported that, solid solution strengthened alloy (Ni–Cr–W–C/Ni–Cr–Mo–Al–C) containing Mo/W in the presence of Cr and C forms different type of carbides based on heat treatment adopted [25, 30–32], which will alter the DRX characteristics and grain size of material during hot deformation. Koundinya et al. [33] have studied the hot deformation behaviour of XH67 (Ni–18.5Cr–4.5Mo–4.5W–3.0Fe–2.5Ti–1.2Al) alloy and identified safe zone of hot working in temperature range of $1100\text{--}1200\text{ }^{\circ}\text{C}$ under $\dot{\epsilon}$ of $0.05\text{--}0.001\text{ s}^{-1}$, and discontinuous DRX as softening mechanism. In precipitation hardened alloys, the presence of secondary strengthening phases such as $\text{Ni}_3(\text{Al}, \text{Ti})$, Ni_3Nb and δ phase have significant influence on softening mechanism [32]. The presence of δ phase in Inconel 718 alloy has resulted in lowering of peak stress requirement,

when specimen was compressed to a strain of more than 0.3 [34]. Most of the literature has focussed on hot workability studies on wrought alloys such as Inconel 718 [34, 35], Inconel 625 [36], Inconel 783 [37] and GH4730 [23], which have comparatively better hot workability than their cast counterparts. It may be noted that in cast alloys, the initiation of DRX mechanism is slower and delayed because of lesser grain boundary area (due to coarser grains) which act as nucleation sites for DRX during hot deformation. From literature, it is understood that very limited studies were reported on the hot workability and dynamic recrystallization behaviour of Ni–Cr–W alloy, and no studies were reported on Ni–25Cr–14W alloy. Therefore, in the present study, the effect of temperature, strain rate and strain on the hot deformation behaviour of double vacuum melted (vacuum induction melting followed by vacuum arc remelted, VIM + VAR) cast ingot of Ni–25Cr–14W alloy has been studied through isothermal hot compression tests. The flow stress data obtained from experiments were analysed mathematically and Arrhenius constitutive equation has been developed for the prediction of flow stress requirement over a wide range of temperatures and strain rates. Based on dynamic material model (DMM), processing map has been prepared and identified the safe region for hot working operations of this alloys based on flow instability criterion. In addition, the present study couples various regions of the processing maps with the corresponding microstructures, obtained from optical as well as electron backscattered diffraction (EBSD), thus enabling a better multiscale understanding of the dynamic recrystallization (DRX) behaviour taking place in the material. Moreover, the multi-step forging experiments, provide a realistic perspective on how partial DRX, arrested due to a sudden drop in the operating temperature and hence the driving force, affect the subsequent mechanical response (hot deformation) of the material. Towards a broader perspective, the analytically derived safe regions for hot working, along with the corresponding microstructural study, provide a better understanding of the Ni–Cr–W solid solution strengthened nickel-based superalloy, which are routinely used in various high-temperature applications in the real world.

Experimental

The material used in the present study is a nickel-based superalloy Ni–25Cr–14W having chemical composition (wt%) given in Table 1. The material has been prepared by VIM followed by VAR. The microstructure, DSC thermogram, XRD spectrum and phase fractions analysed through Thermocalc software for the as-received material are presented in Fig. 1. Cylindrical specimens of $\text{O}10 \times 15\text{ mm}$ were fabricated from the as-cast VIM + VAR ingot for hot compression tests. Isothermal compression tests were performed in the temperature range of $1050\text{--}1200\text{ }^{\circ}\text{C}$ at $50\text{ }^{\circ}\text{C}$ interval, under true strain

TABLE 1: Chemical composition (wt%) of Ni–25Cr–14W superalloy used for the study.

Elements	C	Si	Mn	Cu	Al	Ti	Fe	W	Cr	P	S	Ni
Spec.	0.10 max	0.80 max	0.80 max	0.07 max	0.50 max	0.3–0.7	0.40 max	13–16	23.5–26.5	0.013 max	0.013 max	Bal
Obs.	0.07	0.07	0.01	0.01	0.26	0.52	0.26	14.43	25.22	0.007	0.002	Bal

rates ($\dot{\epsilon}$) of $0.001 - 10 \text{ s}^{-1}$ using a Gleeble 3800 thermomechanical simulator. The temperature control during testing was done in a closed loop control, where the specimen temperature was measured and controlled using K-type thermocouple wires of $\text{Ø}0.25 \text{ mm}$ spot welded on the cylindrical surface at centre of the specimen. The specimen was loaded between two tungsten carbide anvils in Gleeble load train as shown in Fig. 2(a). A thin graphite foil of 5 mil (0.127 mm) thickness was applied with molybdenum disulphide paste at both ends of specimen to have good contact during heating, and minimise the barrelling effect due to reduced friction during hot deformation. The loaded specimen was electrically (joule heating) heated to the desired temperature at a heating rate of 5 °C/sec and soaked for 1 min for temperature uniformity. The specimen was compressed to true strain (ϵ) of ~ 0.75 (corresponding to 50% deformation) and was immediately quenched with water inside the test chamber to retain the microstructure. In order to represent more realistic approach of industrial practice followed during hot deformation, where temperature is not maintained isothermally, but decreases during the deformation start and finish, multi-step forging with varying temperature and strain rates after each step of 0.22ϵ were also performed, as per schematic diagram given in Fig. 2(b). Also, few hot compression samples were further homogenised at 1200 °C for 30 min followed by air cooling prior to hot compression at 1200 °C at varying strain rates, to understand the effects of longer duration homogenisation of hot compression sample.

The load and displacement curves recorded during hot deformation of specimens were used to generate the flow curve (true stress (σ) versus true strain (ϵ)) for different temperatures and strain rates. The flow stress data for different samples were further analysed to understand the strain hardening behaviour and estimated the values of power dissipation efficiency (η), instability parameter (ξ), strain rate sensitivity parameter (m) and activation energy (Q). Processing map for this superalloy was developed for a strain of 0.3 and 0.7 as a function of temperature and strain rate, and various microstructural domains were identified.

Half sectioned deformed specimens were metallographically polished with different grades of silicon carbide emery papers followed by alumina suspension and final polishing was conducted using $1 \mu\text{m}$ diamond paste. The freshly polished specimens were etched with Aqua Regia solution (30 ml HCl + 10 ml

HNO_3) to reveal the microstructural features. Microstructural observations were recorded through Zeiss Lab AX10 microscope. Carl Zeiss Sigma HD field emission gun-scanning electron microscope (FEG-SEM) with energy-dispersive X-ray spectroscopy (EDS) attachment (Oxford Make) was used for identifying the chemistry of cast ingot dendritic arms. In order to obtain finer details of microstructural evolution on deformed samples, electron backscatter diffraction (EBSD) analysis was carried out on selected samples with varying temperature and strain rates. The sample preparation for EBSD analysis was carried out through electropolishing using an 80:20 (ratio) electrolyte solution of methanol and perchloric acid. Stuers™ Lectropol-5 equipment was used for electropolishing at constant temperature of 273 K and voltage of 14 V for 16 s. The EBSD analysis was carried out using FEI™ Quanta 3D-FEG (field emission gun) scanning electron microscope (SEM) equipped with a TSL-EDX™ EBSD system. The confidence index (CI) cut-off of 0.1 was applied during EBSD analysis to have $\sim 95\%$ accuracy in indexing. All EBSD scans reported in this study were performed at a central region of $\sim 300 \mu\text{m} \times 300 \mu\text{m}$, with a step size of $0.2 \mu\text{m}$ and identical beam conditions.

Results and discussion

Characterisation of as-received material

Ni–25Cr–14W is solid solution nickel-based superalloy containing small amount of Al and Ti. The basic composition of this alloy is similar to Haynes 230 [38], with slightly increased content of Cr with addition of Ti. Figure 1(a) shows the typical VIM + VAR processed cast ingot cross-sectional microstructure. The observed microstructure has coarse grains with lamellar dendritic phases around grain boundaries (marked with arrow in Fig. 1(a)). The magnified view of region marked with yellow rectangular box [in Fig. 1(a)] is shown in Fig. 1(b) and observed that regions contain lamella of bright flakes in slightly darker matrix. Figure 1(c) shows the elemental concentration map of Ni and Cr acquired through EDS colour map. The EDS point analysis of matrix (marked as 1) shows Nickel-rich matrix containing Ni–58 (wt%), Cr–26.6 (wt%), and W–14.6 (wt%) with small amount of Ti ~ 0.6 (wt%). The chemical composition of brighter regions (marked with 2) is rich in Cr and contains Cr–45.6 to 56.1 (wt%), W–22.1 to 24.6 (wt%), and Ni – 19.1 to 31.5 (wt%) with small amount of Ti. The sub-matrix around flakes regions

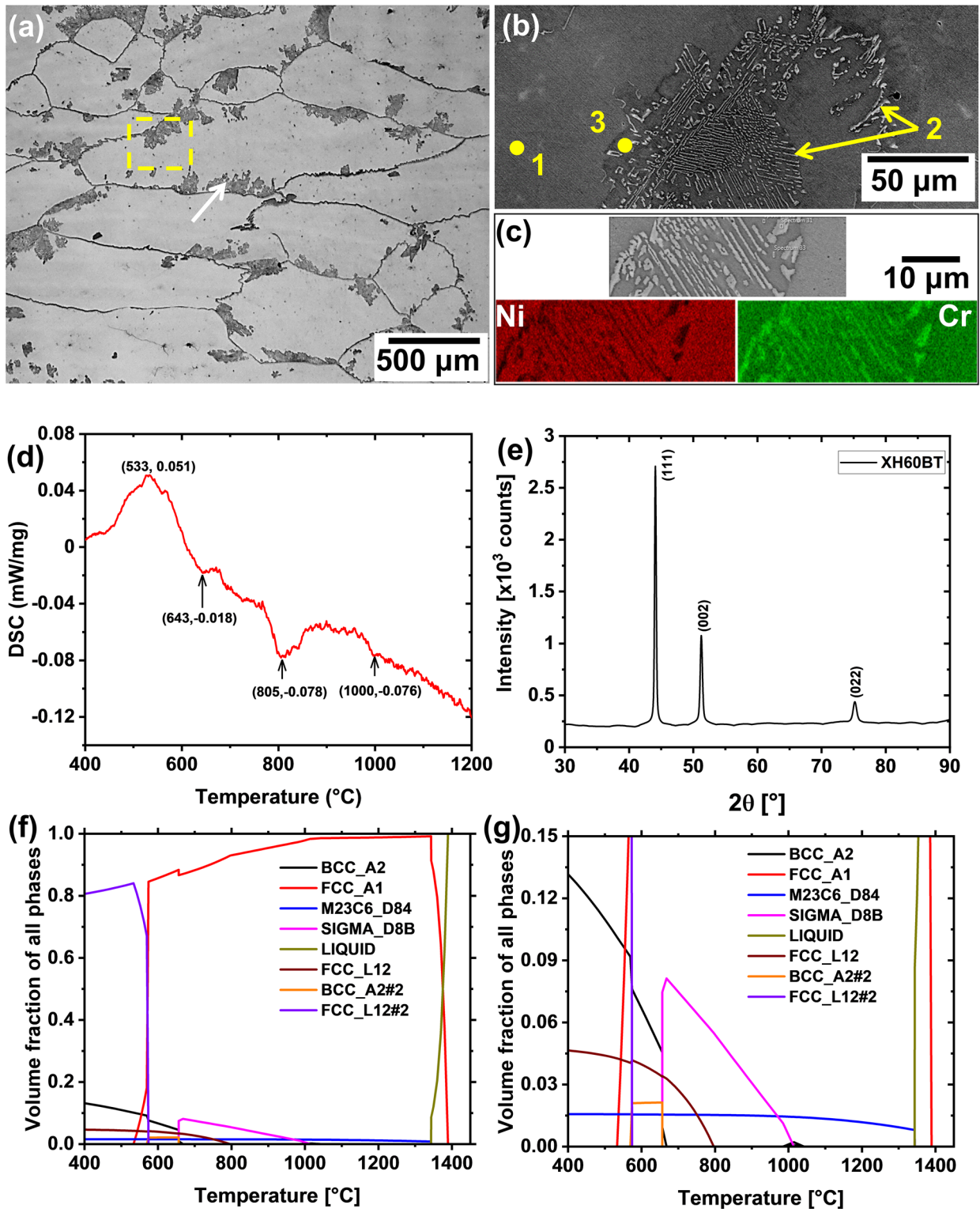


Figure 1: Ni-25Cr-14W cast ingot (a) Optical microstructure of the material showing typical coarse-grained cast structure with a lamellar eutectic phase near the grain boundaries, (b) high-magnification SEM-BSE image of region marked with rectangular box in (a) showing clear lamellae, (c) EDS colour map for Ni and Cr for segregated region, (d) DSC plot with temperature and quantity of energy evolved/absorbed, (e) XRD spectrum of initial cast material, (f) phase fraction analysis through Thermocalc software and (g) zoomed region of phase fractions.

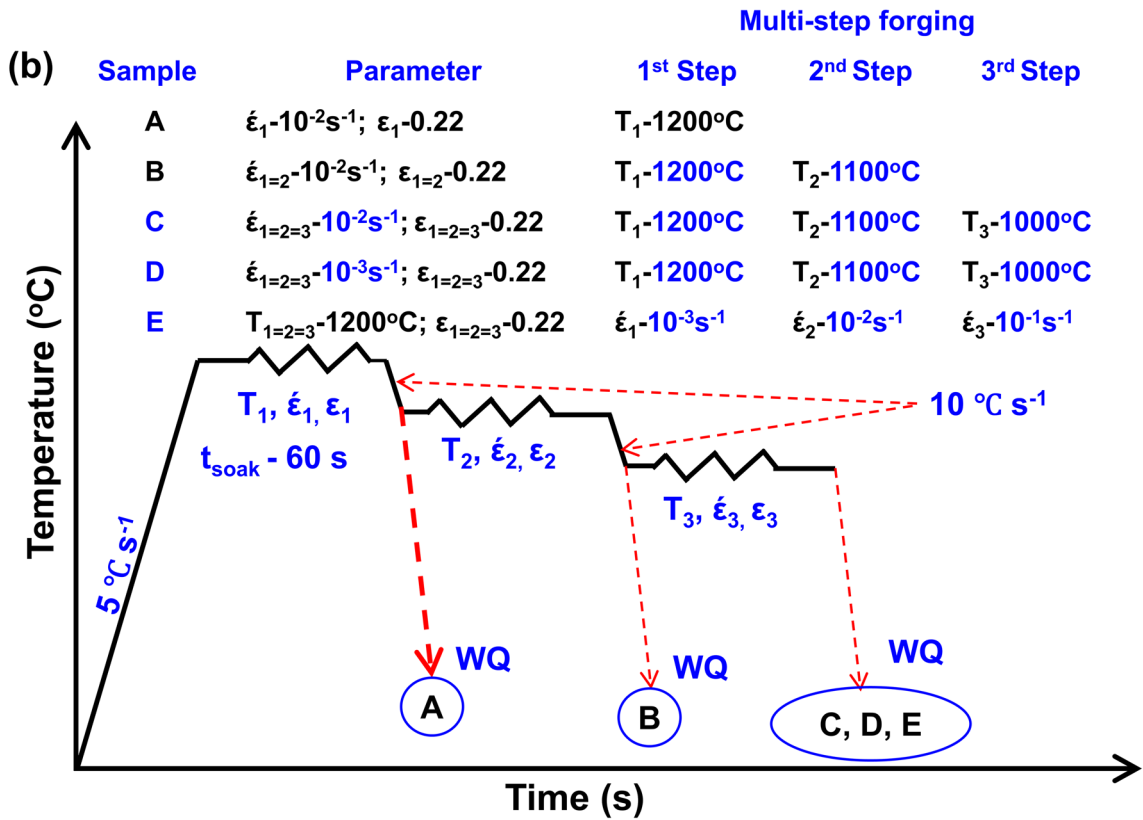
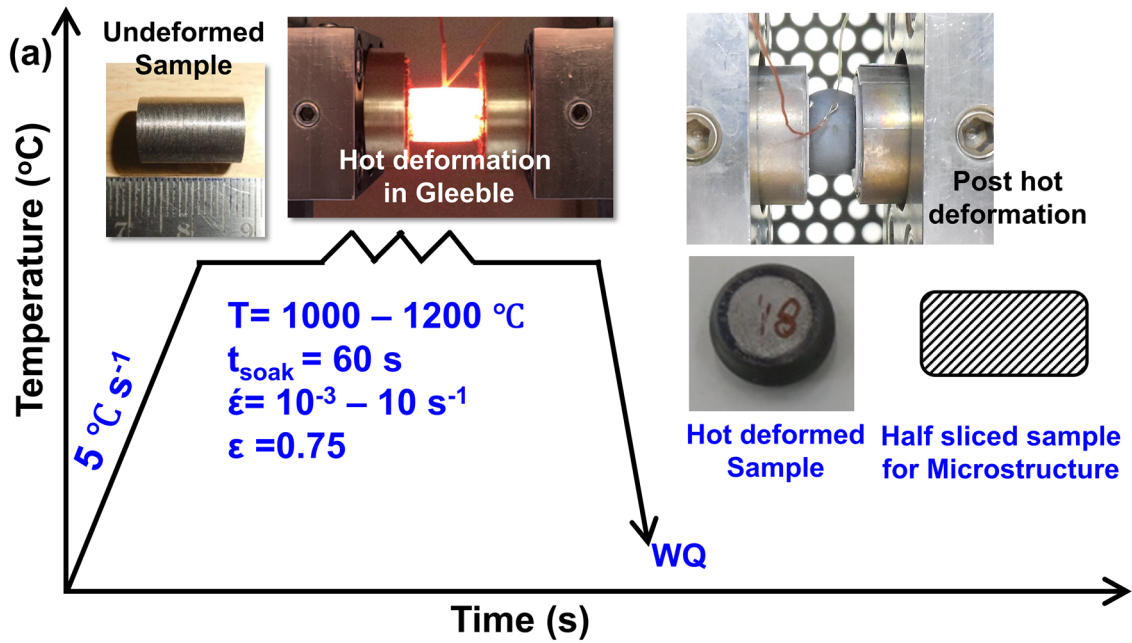


Figure 2: Schematic of experimental plan for (a) Isothermal hot compression test showing details of test conditions and microstructural analysis conducted and (b) multi-step hot compression test performed in Gleeble 3800 thermomechanical simulator.

(marked as 3) which is slightly darker than matrix 1 contains Ni– 55 (wt%), Cr–28.9 (wt%), and W– 14.9 (wt%) with small amount of Ti ~0.6 (wt%). The same trend was noted in EDS colour maps for Ni and Cr shown in Fig. 1(c). Considering the

variations in compositions marked at 1, 2 and 3 [Fig. 1(b) and (c)], it is understood that Cr is segregated at dendritic regions formed during solidification of cast smelt due to variation in cooling rates. Therefore, homogenisation is normally done

to eliminate or reduce the segregation of Cr and W from the matrix, prior to carrying out further thermo-mechanical processing. It was reported that in solid solution [39], the elemental segregation of Cr and W was also observed in solid solution Ni–Co base superalloy. DSC analysis of cast ingot is shown in Fig. 1(d), which shows formation of exothermic peak around 643 °C, indicative of formation low melting phase of σ (D8) phase as confirmed from one-axis phase diagram and equilibrium calculation through ThermoCalc software [Fig. 1(f), (g)]. However, XRD spectrum [Fig. 1(e)] shows peaks corresponding to austenite (γ) matrix only and no others peaks were noticed, which may be due to its small fraction lower than XRD detection limit.

High-temperature flow behaviour (true stress–true strain)

Figure 3 shows the true stress–true strain graphs of hot compression tests of Ni–25Cr–14W alloy for all temperatures at different strain rates. The flow stress values for all temperatures and strain rates are tabulated in supplementary Table S1. Verlinden et al. [40] reported that during dynamic recovery, flow stress saturates after initial period of work hardening, whereas during dynamic recrystallization, flow stress curves have broad peaks or multiple peaks. The extent of DRV and DRX operates during deformation depends on deformation temperature, strain rate

and composition of alloy. In the present study, it is noted that during the initial stage of compression, the flow stress increases rapidly and reaches its peak stress. There is steep rise in the peak stress with strain hardening at $\dot{\epsilon}$ of 10 s^{-1} from 1000 to 1150 °C [Fig. 3(a)–(c)]. A similar trend was observed for $\dot{\epsilon}$ of 1 s^{-1} from 1000 to 1100 °C. Further, it is noted that the reduction in flow stress was observed with increasing temperature, whereas increase in flow stress was noted for increasing $\dot{\epsilon}$. Post peak stress, the behaviour of this alloy can be classified into two types depending on $\dot{\epsilon}$ at which it was deformed. The flow stress gradually decreases when the alloy was deformed at a strain rates of $10\text{--}0.1 \text{ s}^{-1}$. This continuous flow softening at lower temperature of 1000 to 1150 °C with high strain rate of 10 s^{-1} indicates domination of softening caused by dynamic recrystallization over hardening caused by dislocation buildup during increase in strain up to 0.75. The flow instability [24] may be another reason, which is confirmed through microstructural investigation of deformed samples. At strain rate of 0.1 s^{-1} , secondary hardening was observed in the temperature range of 1000 °C to 1150 °C. At slower $\dot{\epsilon}$ of $0.001\text{--}0.01 \text{ s}^{-1}$, the alloy enters a steady flow stress regime due to the balance between dynamic work hardening and dynamic softening, indicative of DRX [16, 41]. The dynamic recrystallization (DRX) process involved formation of strain-free new grains, where nuclei of recrystallized grains are in the part of deformed matrix [42, 43], and involves movement of high-angle grain boundaries. The balance between

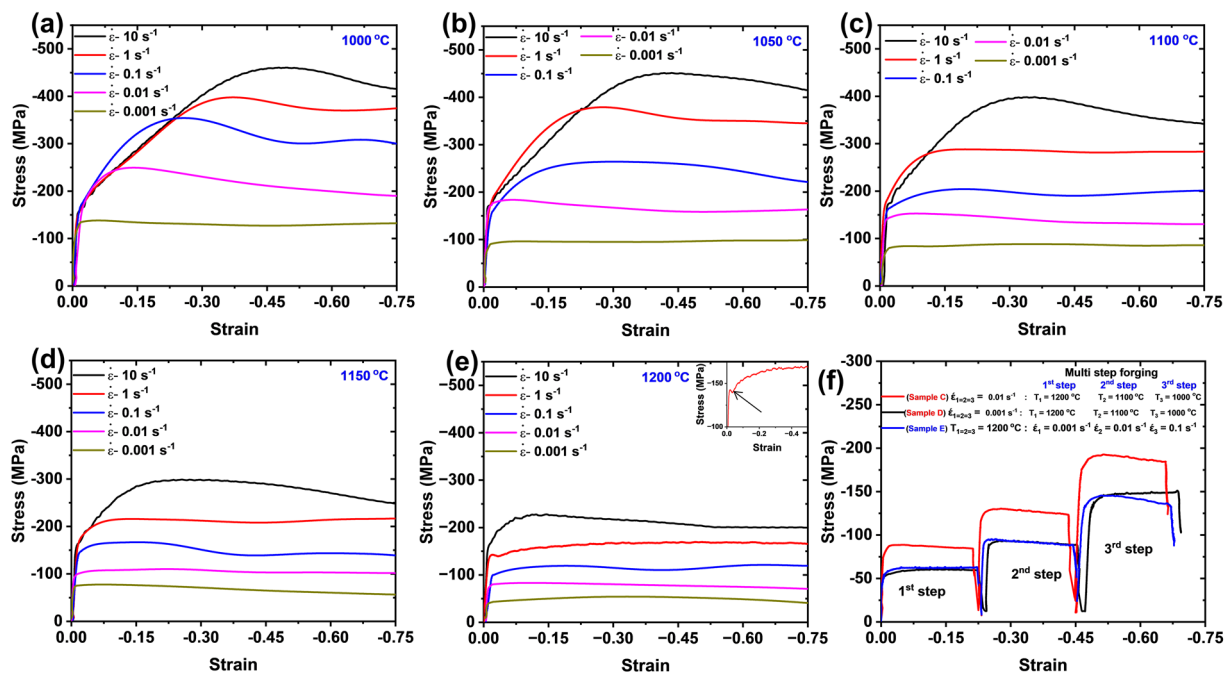


Figure 3: True stress–true strain plots for the Ni–24Cr–14W sample isothermally hot compressed at (a) 1000 °C, (b) 1050 °C, (c) 1100 °C, (d) 1150 °C and (e) 1200 °C, inset shows enlarged view of yield drop phenomena noticed at $\dot{\epsilon}$ of 1 s^{-1} . (f) True stress–true strain plots for the samples deformed at multi-step hot compression by varying temperature or strain rates after each step.

nucleation and growth of the recrystallized grains takes place across deformed microstructure during dynamic recrystallization leading to steady-state flow stress. Flow softening following a peak stress is a result of increase in grain boundary migration rate compared to the nucleation rate, as the boundary of stress free grains spreading to a large volume of deformed region thereby balancing the strain hardening [27]. The DRX is highly sensitive to temperature and depends on the flow stress and the critical strain. At higher temperatures, reduction in the strain hardening is observed due to grain boundary migration and diffusion which reduces the dislocation density and thus reducing the flow stress and critical strain to achieve the DRX. An increase in strain rate of deformation on the other hand reduces the grain boundary migration rate leading to a subsequent increase in dislocation density which eventually increases the flow stress.

One of the interesting features of yield drop phenomena was noted on flow curve of sample deformed at 1200 °C under $\dot{\epsilon}$ of 1 s^{-1} and is shown in Fig. 3(e) inset. Similar phenomena were reported during hot deformation of AD730 alloy [44], Inconel 718, Waspaloy and Haynes 230 [16]. The reasons for same were believed to be short range order locking of dislocations or dislocations pinning by fine particles of γ' and carbides. It may be noted that the present alloy is predominantly strengthened by solid solution strengtheners and carbide formers, as the γ' forming elements (Al and Ti) are minimal and will not be effective at high temperature. Thus, the dislocation pinning by carbides is believed to be the reason for yield drop phenomena in this Ni–25Cr–14W alloy.

Figure 3(f) shows the true stress–true strain diagram for the sample deformed with three step forging done by reducing forging temperature from 1200 °C to 1100 °C to 1000 °C with each step of 0.22 ϵ , at $\dot{\epsilon}$ of 0.001 s^{-1} and 0.01 s^{-1} . Flow behaviour for three step forging carried out by increasing the $\dot{\epsilon}$ from 0.001 s^{-1} to 0.01 s^{-1} to 0.1 s^{-1} at constant temperature of 1200 °C is also shown in Fig. 3(f). It can be seen that the flow curves represent work hardening or dynamic recovery. The certain extent of flow softening or DRX was noted in the third pass for the sample deformed at constant $\dot{\epsilon}$ of 0.01 s^{-1} (sample C) and constant temperature of 1200 °C (sample E). The detail observations towards occurrence of DRX were noted in microstructural investigation and explained in subsequent microstructural section. Values of flow stress increase with lowering of deformation temperature for the sample deformed at 0.001 s^{-1} and same trend with rise in flow stress values was noted for the sample deformed at increased $\dot{\epsilon}$ of 0.01 s^{-1} . For the sample deformed at 1200 °C with increasing $\dot{\epsilon}$ from 0.001 s^{-1} to 0.01 s^{-1} to 0.1 s^{-1} , the flow stress value is similar to the sample deformed at 0.001 s^{-1} with drop in temperature from 1200 °C to 1100 °C to 1000 °C. The above situation is similar to industrial practice, where drop in temperature and variation in strain rates is anticipated during forging. This demonstrates the importance of deciding the

extent of deformation to be imparted to the workpiece in each step under industrial practice.

Figure 4 shows the variation of strain hardening rate ($d\sigma/d\epsilon$) versus flow stress (σ) for samples deformed at 1000–1200 °C. As reported by earlier investigators [45, 46], the occurrence of inversion in the curve is indicative of flow softening and thereby dynamic recrystallization. Inversion is observed for samples deformed at 1000 °C at a $\dot{\epsilon}$ of 10 s^{-1} , 1 s^{-1} , 0.01 s^{-1} and 1050 °C at a $\dot{\epsilon}$ of 0.01 s^{-1} , 0.001 s^{-1} and 1150 °C at $\dot{\epsilon}$ of 10 s^{-1} , 1 s^{-1} , 0.1 s^{-1} and 1200 °C at $\dot{\epsilon}$ of 10 s^{-1} , 1 s^{-1} and 0.1 s^{-1} . In the present case, DRX do happen at slow strain rate of 0.001 s^{-1} as evident from the microstructure observation but there is no inflection point observed in the strain hardening curves since softening behaviour is observed in the flow curve. These observations have been further corroborated by microstructural analysis of deformed samples in Sect. "Microstructural analysis of deformed samples" along with Zener-Hollomon [47] parameter in constitutive analysis Sect. "Development of constitutive analysis", which is a single entity taking into account the effect of strain rate as well as temperature of hot working.

Development of processing map

In order to perform hot working without internal defects, it is essential to have activation of dynamic softening mechanisms during hot deformation and avoid flow instabilities. The activation of softening mechanisms depends on deformation conditions (temperature, strain and strain rate) and in order to identify the optimum conditions. Prasad et al. [24] have developed hot working processing maps based on DMM for different engineering alloys. The processing maps are obtained by superimposition of rheological instability diagram on power dissipation efficiency map. In DMM model, work piece is considered to be a non-linear energy dissipater. The partitioning of input energy (P) into G-content and J-content was decided by strain rate sensitivity (m) of material. The G-content refers to the energy dissipated during hot deformation with generation of heat, whereas J-content represents energy consumed in microstructural evolution during hot deformation. The efficiency of dissipation (η) is determined by comparing J-content with that of an ideal linear dissipater ($m = 1$) [24, 48] as given in Eq. 1.

$$\eta = \frac{J}{J_{max}} = \frac{2m}{m + 1}, \quad (1)$$

where m is the strain rate sensitivity at constant T:

$$m = \frac{\partial \ln(\sigma)}{\partial \ln(\dot{\epsilon})} \quad (2)$$

The flow instability criterion used for constructing processing maps is based on the principles of irreversible thermodynamics of large plastic flow [49] to avoid plastic instability such

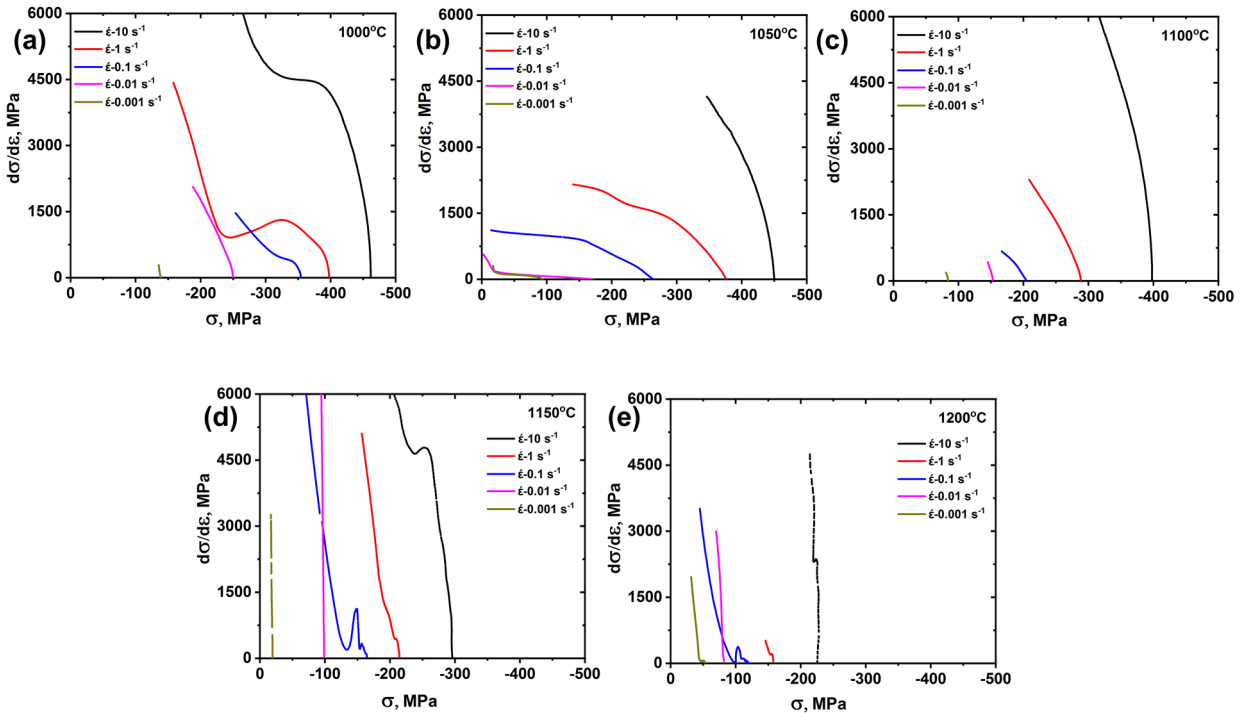


Figure 4: Strain hardening ($d\sigma/d\varepsilon$) versus flow stress (σ) for the samples deformed at different strain rates to $\varepsilon = 0.75$ at (a) 1000 °C, (b) 1050 °C, (c) 1100 °C, (d) 1150 °C and (e) 1200 °C.

as adiabatic shear bands and cracking. Different instability criteria were proposed by various researchers [24, 26, 27]. Based on principles of maximum rate of entropy production [27], the microstructural instability parameter $\xi(\dot{\varepsilon})$ is defined by Eq. 3.

$$\xi(\dot{\varepsilon}) = \frac{\partial \ln[m/(m+1)]}{\partial \ln(\dot{\varepsilon})} + m, \quad (3)$$

where region of $\xi(\dot{\varepsilon}) < 0$ represents flow instability in the processing maps. However, the power dissipation efficiency (η) estimated through Eq. 1 is valid only in case flow stress obeys the power law.

$$\sigma = K(\dot{\varepsilon})^m \quad (4)$$

As the parameter m is independent of $\dot{\varepsilon}$, flow instability criterion (Eq. 3) reduces to $m < 0$. However, this condition is not valid for heavily alloyed material as the flow stress does not obey the power law (Eq. 4) and hence estimation of η and $\xi(\dot{\varepsilon})$. In order to extend the flow behaviour for materials which do not obey power law, the instability criterion was modified by Murty et al. [27] and represented by Eq. 5.

$$2m < \eta \leq 0 \quad (5)$$

For the stable material flow, $0 < \eta < 2m$, where m values lie between 0 and 1 and derived from theoretical considerations of the maximum power dissipation rate by material systems and experimental values. However, the instability condition of $\eta \leq 0$

seems to violate the feasibility conditions for the instabilities to occur, since at a given temperature, net dissipative work in the hot working regime is directly proportional to the internal entropy of the material which is positive in case of irreversible processes [48].

$$P = \sigma \dot{\varepsilon} = T \frac{dS}{dT} \geq 0 \quad (6)$$

Hence, the ratio of dissipative power to net dissipative work should also be positive. This can also be depicted by area under stress-strain curves, where the ratio of J/J_{max} bears a positive value. Hence, the instability domain has been redefined as written in Eq. 7 and $\eta \leq 0$ can be neglected while calculating the boundaries of instability domains:

$$\xi = \frac{2m}{\eta} - 1 \leq 0; m \notin (0, 1) \quad (7)$$

The strain rate sensitivity (m) map, processing map superimposing instability criteria and activation energy maps of Ni-25Cr-14W alloy for strain values of 0.3 and 0.7 are plotted in Fig. 5(a)-(f), respectively. From m map, the maximum value of m corresponding to ε of 0.3 is 0.25 in the temperature range of 1000–1050 °C at low $\dot{\varepsilon}$ of 0.001 s⁻¹, with increase in extent of strain to 0.7, additional temperature region (1150–1200 °C) was noted with similar value of m . The processing maps [Fig. 5(c), (d)] exhibited maximum efficiency in the region having maximum value of m as observed

in Fig. 5(a), (b). The processing map corresponding to higher deformation with ϵ of 0.7 is considered as more realistic with steady-state condition for the material during processing. The ‘safe’ region has been identified in the temperature range

of 1000–1200 °C and strain rates of 0.001–0.1 s⁻¹ with maximum efficiency of ~ 44% at 1175 °C and 0.001 s⁻¹. Based on flow curve analysis [Fig. 3(a)–(e)], which exhibit typical DRX feature for low strain rates, this region can be interpreted to

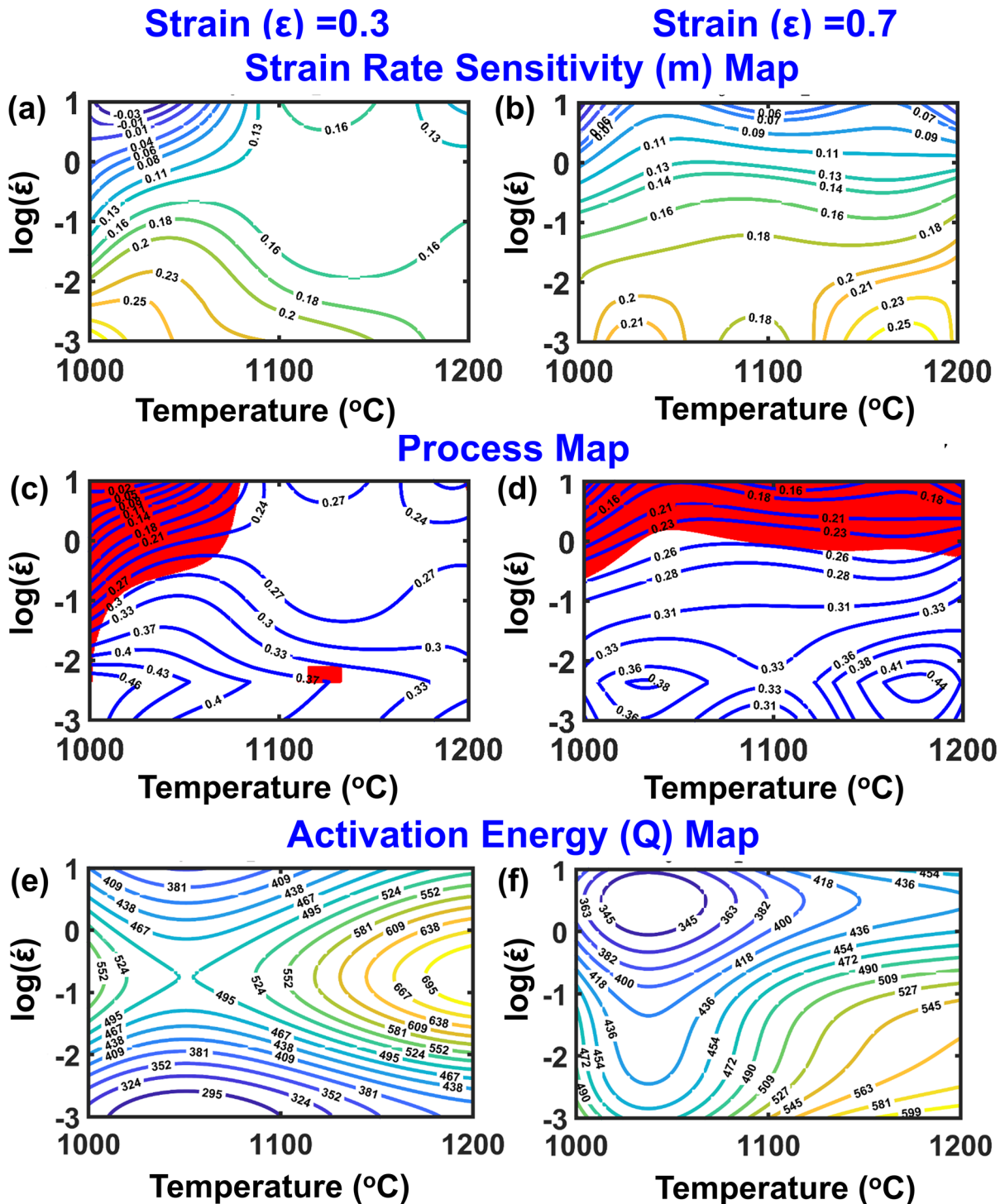


Figure 5: Contour map of (a, b) strain rate sensitivity parameter (m), (c, d) efficiency of power dissipation (η) with superimposed instability criterion, and (e, f) activation energy (Q) for strain of $\epsilon=0.3$ (a, c and e) and $\epsilon=0.7$ (b, d and f), respectively.

be the regime of dynamic recrystallization. At higher temperatures, microstructural re-constitution increases, and similar observation was reported by Liu et al. [16] during hot working of Ni–Cr–W alloy. For smaller amount of deformation ($\epsilon = 0.3$) and higher strain rates up to 10 s^{-1} , the processing map shows stable region with lower η values. The ‘unstable’ region was identified based on instability criterion (Eq. 7) and found to occur when sample is deformed at higher $\dot{\epsilon}$ $1\text{--}10 \text{ s}^{-1}$ in temperature range of $1000 \text{ }^\circ\text{C}$ and above. Figure 5(e), (f) shows the contour map of activation energy with varying temperatures and strain rates, for the sample deformed up to strains of 0.3 and 0.7, respectively.

Microstructural analysis of deformed samples

Figure 6 shows the complete spectrum of optical micrographs of hot compressed samples of Ni–25Cr–14W alloy. Water quenching was performed post hot compression tests to retain the elevated temperature deformed microstructures. Pancaked features were observed in the samples deformed at low temperature ($< 1150 \text{ }^\circ\text{C}$) and high strain rates ($\dot{\epsilon}$ $0.1\text{--}10 \text{ s}^{-1}$), indicating strain hardening during deformation. The onset of recrystallization

near the grain boundaries was noted for the sample deformed at $1000 \text{ }^\circ\text{C}$ with high $\dot{\epsilon}$ of 10 s^{-1} and the extent increases with reduction in $\dot{\epsilon}$ to 0.001 s^{-1} or increases in deformation temperature to $1200 \text{ }^\circ\text{C}$. With increase in temperature, dynamic softening behaviour gets activated leading to more number of nucleated grains and subsequent growth of these newly formed grains during deformation at slow strain rate 0.001 s^{-1} , as can be observed from the sample deformed at $1200 \text{ }^\circ\text{C}$. The microstructure of the sample homogenised for longer duration (30 min) and subsequently deformed at $1200 \text{ }^\circ\text{C}$ under varying $\dot{\epsilon}$ is shown in last column in Fig. 6, which reveals similar features to that of $1200 \text{ }^\circ\text{C}$ sample, deformed without any long-term homogenisation.

Figure 7(a)–(i) and Fig. 7(j)–(r) shows the EBSD inverse pole figure (IPF) and kernel average misorientation (KAM) maps, respectively, of the samples deformed at $\dot{\epsilon}$ of 0.001 s^{-1} by varying the temperature in the range of $1000\text{--}1200 \text{ }^\circ\text{C}$, and at $1200 \text{ }^\circ\text{C}$ at different $\dot{\epsilon}$ of $10\text{--}0.001 \text{ s}^{-1}$. A change in recrystallization fraction and grain size variation was noted with respect to change in temperature and strain rates. From Fig. 7(a)–(c), it is noted that sample deformed at temperature of $\leq 1100 \text{ }^\circ\text{C}$ has elongated grains with appearance of limited DRX grains with high -angle grain boundary (HAGB) at initial original grain

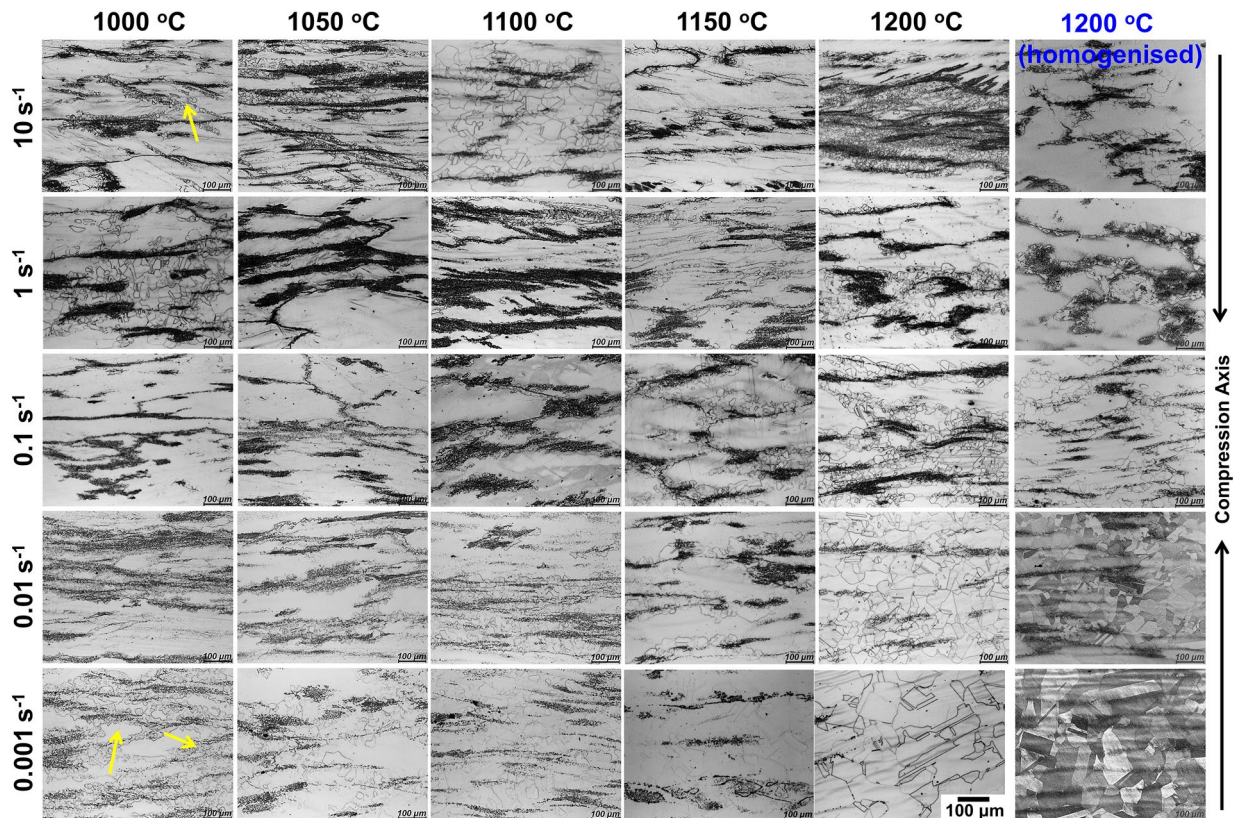


Figure 6: Optical microstructures of Ni–24Cr–14W as-cast sample after hot compression ($\epsilon = 0.75$) tests performed in the temperature range of $1000\text{--}1200 \text{ }^\circ\text{C}$ and $\dot{\epsilon}$ of $0.001 \text{ s}^{-1}\text{--}10 \text{ s}^{-1}$. Microstructures of samples homogenized and subjected to hot deformation at $1200 \text{ }^\circ\text{C}$ with varying $\dot{\epsilon}$ are shown in last column.

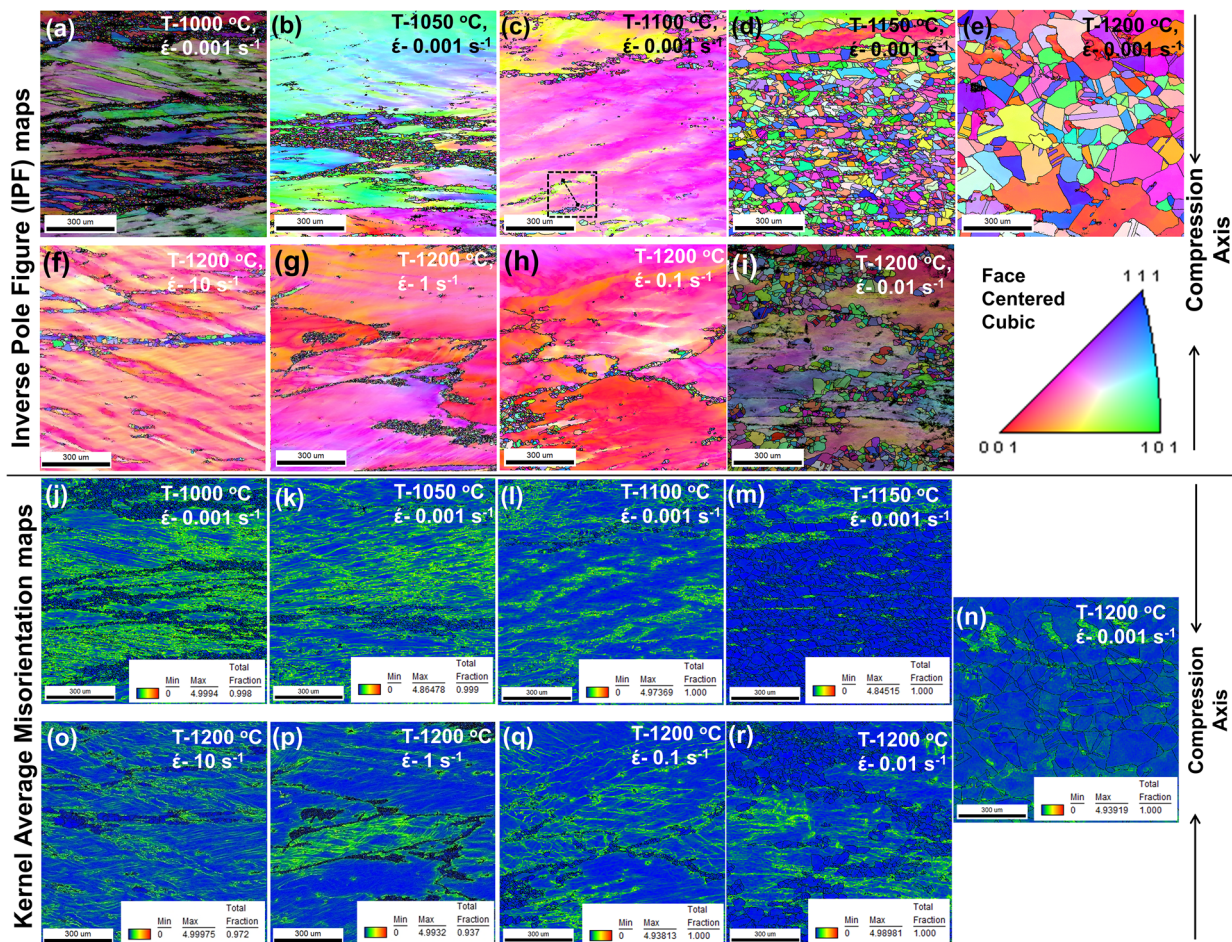


Figure 7: Inverse Pole Figure (IPF) maps of sample deformed to $\epsilon=0.75$ under $\dot{\epsilon}=10^{-3} \text{ s}^{-1}$ at (a) 1000 °C, (b) 1050 °C, (c) 1100 °C, (d) 1150 °C and (e) 1200 °C. IPF of sample deformed to $\epsilon=0.75$ at 1200 °C under varying strain rates (f) 10 s^{-1} , (g) 1 s^{-1} , (h) 0.1 s^{-1} and (i) 0.01 s^{-1} . The corresponding Kernel Average Misorientation maps for Fig. (a–i) are shown in Fig. (j–r), respectively. The misorientation profile along the black marker in Fig. 7(c) is shown in supplementary Fig. S1.

boundaries. With increase in deformation temperature to 1150 °C and above [Fig. 7(d), (e)], the size and amount of recrystallized grains have been increased appreciably. The variation in recrystallized grains size at different temperature is plotted in Fig. 8. The recrystallization fraction was estimated with GOS threshold criteria, where $\text{GOS} < 0.75^\circ$ are considered as recrystallized grains [50]. The presence of orientation gradient due to lattice rotation are interpreted with colour gradients observed in the IPF maps [32], whereas, local lattice rotation represented by point-to-point misorientation is interpreted with KAM maps. This is frequently applied to highlight the strain localizations in microstructures and denotes the average misorientation of given pixel with its immediate neighbours. Procedural aspect for KAM analysis is explained in earlier studies [51, 52]. The KAM maps [Fig. 7(j)–(r)] show the sub-structural evolution across the grain and dislocation density, and sample having more recrystallized grains has lower KAM value, due to less misorientation among recrystallized grains.

In conjunction with flow curves, optical microstructure and EBSD (IPF and KAM) analysis, it is inferred that hot deformation at $\dot{\epsilon} 0.001 \text{ s}^{-1}$ up to 1100 °C and deformation at 1200 °C up to $\dot{\epsilon} 0.01 \text{ s}^{-1}$ show higher fraction of coarse grains with colour gradient in microstructure. Microstructure shown in Fig. 7(a)–(c) and Fig. 7(f)–(i) typically shows partial DRX, where newly formed grains are distributed around deformed initial large grains, showing a typical “necklace structure” [25, 53]. KAM maps suggest higher dislocation densities around serrated grain boundaries, indicative of DRX through discontinuous dynamic recrystallization (DDRX) [32]. It is also noted from IPF [Fig. 7(i)] map that the sample deformed at 1200 °C under $\dot{\epsilon}$ of 0.01 s^{-1} shows fine recrystallized grains, embedded within the larger deformed grains in the microstructure at few locations. Such type of recrystallized grains is often attributed to Continuous DRX mechanism (CDRX), where the subgrains progressively rotate to form DRX grains within the parent grains [54]. The reader is referred to supplementary Fig. S1, where

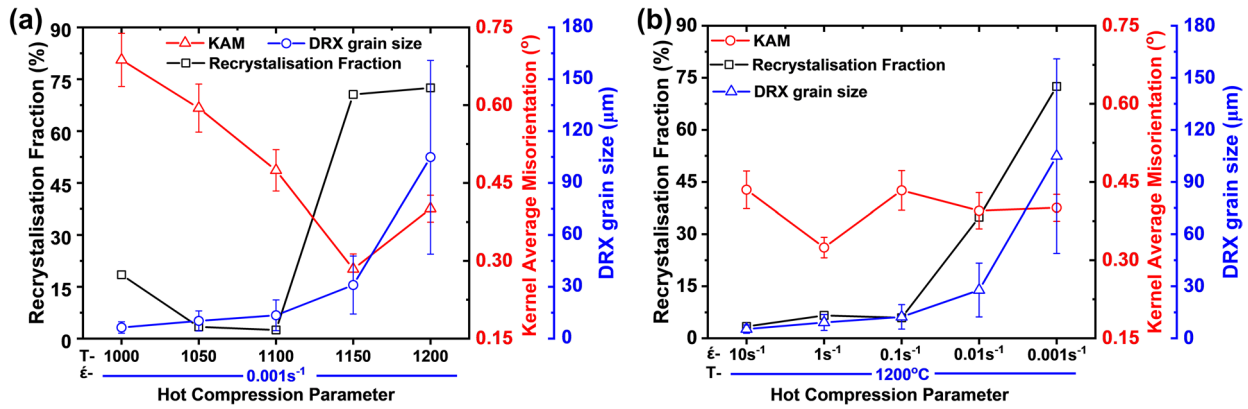


Figure 8: Plots showing the volume fraction of dynamically recrystallized grains, Kernel average misorientation and dynamically recrystallized grain size as a function of deformation conditions for the samples deformed to $\epsilon=0.75$ at (a) varying temperatures under $\dot{\epsilon}$ of 0.001 s^{-1} , and (b) at $1200\text{ }^{\circ}\text{C}$ with varying $\dot{\epsilon}$.

line profile analysis of misorientation development across these subgrains has been studied. Two particular misorientation measures, ‘point to point’ and ‘point to origin,’ have been plotted (see Fig. S1) across the analysis path (see black markers) provided in Fig. 7(c). The ‘point to origin,’ which is indicative of the misorientation accumulation along the analysis path with respect to the orientation at the line origin, shows a gradual increase up to over 12° . The lack of sufficient nucleation sites at the grain boundaries further promotes the CDRX mechanism in such coarse-grained microstructures. Similar observations were reported elsewhere during hot deformation of cast Ni–Cr–W alloy [16], CoNi superalloy [20] and inferred that in as-cast coarse-grained microstructures, nucleation sites for DRX are comparatively less because of lower grain boundary area. Therefore, nucleation of DRX also takes place inside the grains. KAM map further shows sub-structural feature on the sample deformed at lower strain rate $\dot{\epsilon}$ of 0.001 s^{-1} , indicating higher dislocation density across the grains, rather than grain boundary alone on the sample deformed at $T < 1150\text{ }^{\circ}\text{C}$ or $\dot{\epsilon} > 0.01\text{ s}^{-1}$. Considering above, it is inferred that these sub grains may have formed through sub-grain rotation [32, 36], indicating multiple DRX mechanisms operating in this alloy.

From Fig. 8(a), for the samples deformed to ϵ of 0.75 at constant $\dot{\epsilon}$ of 0.001 s^{-1} , it is noted that the volume fraction of recrystallization increases with rise in deformation temperature and obtained about 70% recrystallized grains with average recrystallized grain size of $31 \pm 17\text{ }\mu\text{m}$ at $1150\text{ }^{\circ}\text{C}$. The recrystallized grain size (d_{DRX}) observed for the sample deformed at $1200\text{ }^{\circ}\text{C}$ is $104 \pm 56\text{ }\mu\text{m}$ with recrystallization fraction of 72.5%. This is because increased deformation temperature has provided sufficient driving force for grain boundary migration and thus acceleration of DRX process. Similarly, Fig. 8(b) shows the effect of variations in $\dot{\epsilon}$ on recrystallization fraction and grain size of the samples deformed at constant temperature of $1200\text{ }^{\circ}\text{C}$ with

ϵ of 0.75. It can be noted that, in spite of high temperature, samples deformed at $\dot{\epsilon} > 0.01\text{ s}^{-1}$ have recrystallization fraction less than 6.6%, which has increased to 35% and 72.5% for lower $\dot{\epsilon}$ of 0.01 s^{-1} and 0.001 s^{-1} , respectively. For given temperature of $1200\text{ }^{\circ}\text{C}$, deformation at higher strain rate results in increase in dislocation density and materials preserve a majority of deformation energy within grains, which results in high nucleation rates of recrystallization, but have little deformation time for the growth of DRX nuclei [20, 55, 56]. With deformation at lower strain rates ($\dot{\epsilon} < 0.01\text{ s}^{-1}$), deformation time increases, which provides sufficient time for the formation of new DRX nuclei throughout the matrix, growth of DRX grains and further deformation of previously formed DRX grains. Due to this, formed microstructure consists of dynamic mixture of grains with different dislocation densities and increase in DRX fraction as evident from Figs. 7(e) and 8(b) for the sample deformed at $1200\text{ }^{\circ}\text{C}$ at strain rates of 0.001 s^{-1} . At higher strain rates, domination of work hardening was observed from flow diagram [Fig. 3(e)].

Figure 9 shows the image quality map, IPF map and KAM map for the samples deformed with multi-step hot compression, where deformation temperature after each step of $\epsilon 0.22$ has been reduced by $100\text{ }^{\circ}\text{C}$ from start temperature of $1200\text{ }^{\circ}\text{C}$ to finish temperature of $1000\text{ }^{\circ}\text{C}$ and compressed at 0.01 s^{-1} and 0.001 s^{-1} . In third set [Fig. 9(g)–(i)], temperature was maintained constant at $1200\text{ }^{\circ}\text{C}$, but the strain rate was increased from 0.001 s^{-1} to 0.01 s^{-1} and finally to 0.1 s^{-1} . However, all deformed samples showed initiation of DRX, especially at grain boundaries, at the end of multi-step forging experiments. These microstructures indicate partial DRX (Fig. 9), as the sample has not been recrystallized throughout and the process has been limited to only a finite region, in the vicinity of grain boundaries. The mechanical response profiles shown in Fig. 3(f), however, do not show a significant dynamic softening. This can be attributed to two specific reasons, (a) the fraction of overall microstructure recrystallized

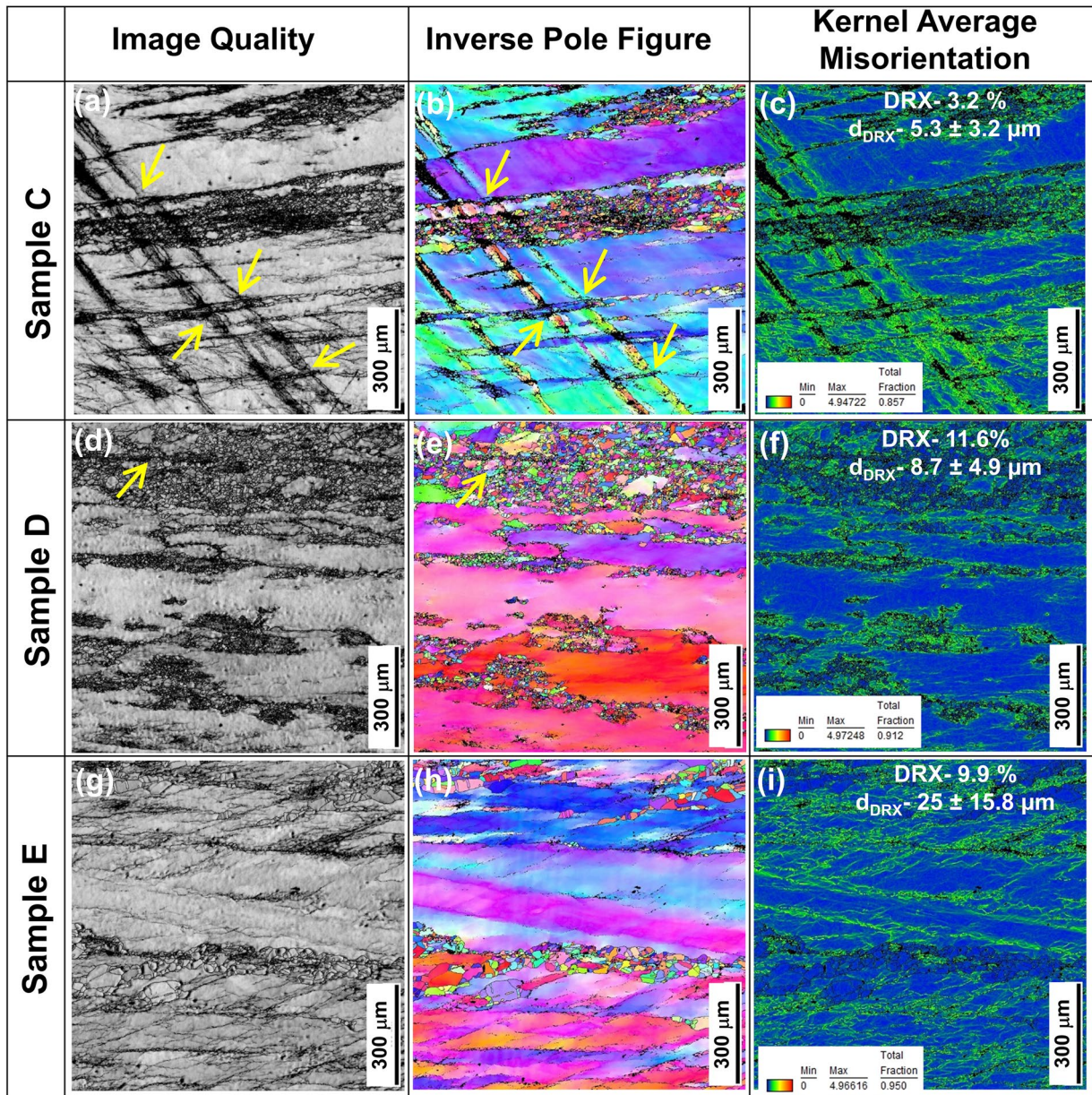


Figure 9: EBSD Image Quality map (a, d, g), Inverse Pole maps (IPF) (b, e, h) and Kernel Average Misorientation maps (c, f, i) for three step hot compressed samples [C, D of Fig. 2(b)] deformed at (a–c): $\dot{\epsilon} = 0.01s^{-1}$ and (d–e) $\dot{\epsilon} = 0.001s^{-1}$ with reduction in temperature by 100 °C from 1200 °C after each step ($\epsilon \sim 0.22$), and (g–i) sample E of Fig. 2b deformed at 1200 °C with change in $\dot{\epsilon}$ from $0.001s^{-1}$ to $0.01s^{-1}$ to $0.1s^{-1}$ after each step ($\epsilon \sim 0.22$). The reader is referred to Sect. "Microstructural analysis of deformed samples" for description on markers used in a,b,d,e.

in each of these is significantly lower, with a maximum magnitude of $\sim 11.6\%$. The contribution from the non-recrystallized regions hence dominates the mechanical response curve and lower the fractional softening [57]; (b) Once the critical strain for DRX has been achieved [43], the DRX grains begin to nucleate. However, the progressive deformation followed by a sudden drop in the temperature restricts their growth. In parallel, the progressive deformation results in a significant misorientation accumulation, even within these newly formed grains [see Fig. 9(a)–(i)].

The dynamic softening due to the newly formed strain-free recrystallized grains is overcome by the strain hardening taking place within these grains as a result of the significant imposed deformation. This is also evident from the large misorientation accumulation seen in the band of DRX grains in Fig. 9(c), (f). Such a phenomenon results in rise of the steady-state stress observed in the mechanical response curve in Fig. 3(f).

It is important to note here that the stripes present across the EBSD micrographs shown in Fig. 9(a)–(c) are strain

localizations, more specifically, the shear bands that have formed as a result of the hot deformation process. A significant orientation gradient can be seen across these strain localizations in the IPF as well as KAM maps shown in Fig. 9(b), (c). Such instabilities arise due to a sudden decrease in the temperature during multi-step forging; thus, localizing the otherwise homogeneous deformation that would have taken place, if there were no temperature variations during the multi-step forging process [see Fig. 7(e)]. On the other hand, these strain localizations, more specifically, their intersections with grain boundaries, act as nucleation sites for the DRX grains, see yellow markers in Fig. 9(b), (e). The stored energy accommodated by these bands acts as driving force for the DRX grains. However, it is to be noted that the sudden temperature drop further hinders the growth of these DRX grains.

Development of constitutive analysis

As the hot deformation process is thermally activated process, the peak stress variation with respect to deformation temperature, strain and strain rates are estimated through classical Arrhenius-type equations [29]. This is further used to estimate the activation energy to predict the mode of deformation mechanism during hot deformation [16, 25, 37].

$$\dot{\epsilon} = A_1 \sigma^{n_1} \exp\left(\frac{-Q}{RT}\right) \quad (8)$$

$$\dot{\epsilon} = A_2 \exp(\beta\sigma) \exp\left(\frac{-Q}{RT}\right) \quad (9)$$

$$\dot{\epsilon} = A_3 [\sinh(\alpha\sigma)]^n \exp\left(\frac{-Q}{RT}\right), \quad (10)$$

where $\dot{\epsilon}$ is strain rate, σ is flow stress, $A_1, A_2, A_3, n_1, n, \alpha$ and β are material constants and $\alpha = \beta/n_1$, R is gas constant (8.314 J/mol-K), T is deformation temperature (K) and Q is apparent hot deformation activation energy (kJ/mol), which represents the energy barrier to dislocation slip during hot deformation. The extent of difficulty during hot deformation can be interpreted through the value of Q , where higher value of Q in Ni alloys indicates more difficulty during hot working [21]. The power law Eq. 8 and exponential law Eq. 9 are mainly used to describe hot deformation behaviour in low stress ($\alpha\sigma < 0.8$) and high stress ($\alpha\sigma > 1.2$) regimes, respectively [35]. The hyperbolic-sine function given in Eq. 10 was proposed by Sellars and McTegart [58] and applicable for all ranges of stress, and therefore was selected to describe the hot deformation behaviour of Ni-25Cr-14W superalloy in this study.

In order to calculate the parameters of Eq. 10, some mathematical treatments were performed, as explained in earlier study [20, 25, 35, 36]. The values of β and n_1 are obtained from linear

fitting plot of experimental data of $\ln \dot{\epsilon}$ versus σ and $\ln \dot{\epsilon}$ and $\ln \sigma$, and given in supplementary Fig. S2a and Fig. S2b, respectively. The value of $\alpha (= \beta/n_1)$ was estimated from average values of β and n_1 , which are estimated by averaging the values of β and n_1 obtained at each temperature. The Eq. 10 has been rewritten (Eq. 11) after taking logarithm on both sides.

$$\ln \dot{\epsilon} = \ln A_3 + n \ln[\sinh(\alpha\sigma)] - \frac{Q}{RT} \quad (11)$$

The linear fitting slope of $\ln \dot{\epsilon}$ versus $\ln[\sinh(\alpha\sigma)]$ (supplementary Fig. S2c) at constant temperature gives the value of n . At a constant strain rate, the activation energy Q is determined by Eq. 12.

$$Q = Rn \frac{\partial \ln[\sinh(\alpha\sigma)]}{\partial (1/T)}, \quad (12)$$

where $\frac{\partial \ln[\sinh(\alpha\sigma)]}{\partial (1/T)}$ is estimated from linear fitting plot of $\ln[\sinh(\alpha\sigma)]$ versus $1/T$ (supplementary Fig. S2d).

As the hot deformation is thermal activated process, many researchers have used peak stress [35, 37] and steady-state stress [16, 28] for the estimation of apparent activation energy (Q). In the present case, steady-state flow stress values at different temperature, strain rates ($\dot{\epsilon}$) corresponding to true strain of 0.7 have been used. Based on test data, the apparent activation energy has been calculated as 472 kJ/mol for this Ni-25Cr-14W alloy. This estimated value is closed to the reported activation energy of 456 kJ/mol of cast Ni-Cr-W alloy [16] containing Mo and La. This higher value of activation energy compared to Ni self-diffusion activation energy (292 kJ/mol) is due to solid solution strengthening effect of Cr and W in nickel. This computed apparent activation energy of 472 kJ/mol is comparatively lower than the apparent activation energy of 520 kJ/mol of cast Inconel 620 alloy [25], indicating more easiness during hot working of this alloy. It should also be noted that cast alloy has relatively higher activation energy compared to wrought alloy of Inconel 783 (445 kJ/mol) and ATI 718 plus (466 kJ/mol) [35, 37].

In order to validate the constitutive equation and understand the flow behaviour, Zener-Holloman parameter (Z) is introduced by Eq. 13, which is temperature compensated strain rate and provides synergistic effect of strain rate and deformation temperature [22, 35] and considered as sign of validity [37] of constitutive equation.

$$Z = \dot{\epsilon} \exp\left(\frac{Q}{RT}\right) = A_3 [\sinh(\alpha\sigma)]^n \quad (13)$$

Taking logarithm on both sides of the Eq. 13.

$$\ln Z = \ln A_3 + n \ln[\sinh(\alpha\sigma)] \quad (14)$$

The values of Z are calculated by using the previously computed average value of ' Q ' using first part of Eq. 13 corresponding to temperatures (T) and strain rates ($\dot{\epsilon}$). The slope

of the linear fit of $\ln Z$ and $\ln[\sinh(\alpha\sigma)]$ as shown in the supplementary Fig. S2(e) provides the value for the constants A_3 and n . The linear fitting line shows good correlation between $\ln Z$ versus $\ln[\sinh(\alpha\sigma)]$ with correlation coefficients of 0.998 for Ni-25Cr-14W alloy.

Based on the estimated values of the A_3 , α , n and Q , the constitutive relationship between stress and strain rate has been established for Ni-25Cr-14W alloy using Eq. 10.

$$\dot{\epsilon} = 2.172 \times 10^{16} [\sinh(0.00608\sigma)]^{4.53} \left[\exp\left(\frac{-472.13 \times 10^3}{RT}\right) \right] \quad (15)$$

Based on above, flow stress has been rewritten as hyperbolic-sine function by Eq. 16 and by substituting the values of parameters flow stress has been predicated.

$$\sigma = \frac{1}{\alpha} \ln \left\{ \left(\frac{Z}{A_3} \right)^{\frac{1}{n}} + \left[\left(\frac{Z}{A_3} \right)^{\frac{2}{n}} + 1 \right]^{\frac{1}{2}} \right\} \quad (16)$$

Scatter plot of experimental flow stress and predicted flow stress through constitutive equation is shown in supplementary Fig. S2(f). The data points have slope of 0.987, indicative of close prediction of flow stress through constitutive equation.

In order to understand the flow curve and microstructural perspective in terms of Zener-Hollomon (Z) parameter [47], it is understood that drop in flow stress curves, shown in Fig. 3, from σ_{peak} to σ_{SS} or the steady-state stress increases with an increase in Z . This is because higher Z , which implies higher imposed strain rate, results in an enhanced dislocation density reduction, thus resulting in a significant increase in $\sigma_{peak} - \sigma_{SS}$ [47]. The corresponding work-hardening behaviour of these curves, shown in Fig. 4, also indicates a similar dependence on the Zener-Hollomon parameter Z . From a microstructural perspective, however, lower Z which implies higher temperature and lower strain rate provides a sufficient driving force for the newly formed DRX grains to grow completely, thus leading to a fully recrystallized microstructure.

Strain-compensated constitutive equation

In ideal case, the calculated parameters of the constitutive equation are constant and are independent of strain. However, in practice, the effect of strain on constitutive equation parameters should not be ignored. Therefore, in order to account for the strain on each parameter to improve the accuracy of constitutive model [35, 45, 59], the values of parameters Q , n , α and $\ln A_3$ have been estimated at different values of strain in the range of 0.1 to 0.7 covering full spectrum of flow behaviour. The functional mathematical relationship between all parameters and

strain is expressed by quadrinomial fitting (polynomial of fourth order) and expressed by Eqs. 17 to 20.

$$Q = Q_0 + B_1\epsilon + B_2\epsilon^2 + B_3\epsilon^3 + B_4\epsilon^4 \quad (17)$$

$$n = n_0 + C_1\epsilon + C_2\epsilon^2 + C_3\epsilon^3 + C_4\epsilon^4 \quad (18)$$

$$\alpha = \alpha_0 + D_1\epsilon + D_2\epsilon^2 + D_3\epsilon^3 + D_4\epsilon^4 \quad (19)$$

$$\ln A_3 = E_0 + E_1\epsilon + E_2\epsilon^2 + E_3\epsilon^3 + E_4\epsilon^4 \quad (20)$$

The plot of Q , n , α and $\ln A_3$ as a function of strain is plotted in supplementary Fig. S3(a)-(d). After substituting the values of constants, polynomial equations have been rewritten (21-24).

$$Q = 309.9 + 755.3\epsilon - 430.0\epsilon^2 - 1841.8\epsilon^3 + 1984.4\epsilon^4 \quad (21)$$

$$n = 6.88 - 17.14\epsilon + 44.50\epsilon^2 - 50.69\epsilon^3 + 21.44\epsilon^4 \quad (22)$$

$$\alpha = 0.00732 - 0.0117\epsilon + 0.02488\epsilon^2 - 0.01592\epsilon^3 - 0.000897\epsilon^4 \quad (23)$$

$$\ln(A_3) = 25.91 + 40.24\epsilon + 60.41\epsilon^2 - 314.28\epsilon^3 + 257.31\epsilon^4 \quad (24)$$

From supplementary Fig. S3, the effect of strain on constitutive equation parameters has been understood. With increase in strain value, stress index n decreases [Fig. S3(b)] and then becomes stable indicating reduction in stress sensitivity. The value of apparent activation energy [Fig. S3(a)] increases with strain, signifying difficulty of alloy with more deformation. The variation of α and $\ln A_3$ is shown in Fig. S3(c) & S3(d), respectively. After substituting these constitutive equation parameters in Eq. 16, the flow stress constitutive equation can be rewritten as Eq. 25.

$$\sigma = \frac{1}{\alpha(\epsilon)} \ln \left\{ \left(\frac{Z}{A_{3(\epsilon)}} \right)^{\frac{1}{n(\epsilon)}} + \left[\left(\frac{Z}{A_{3(\epsilon)}} \right)^{\frac{2}{n(\epsilon)}} + 1 \right]^{\frac{1}{2}} \right\} \quad (25)$$

Conclusions

Hot deformation study of Ni-25Cr-14W superalloy has been carried at 1000–1200 °C under strain rates of 0.001–10 s⁻¹. The following are the major conclusions drawn from the study:

- (1) Ni-25Cr-14W alloy exhibits stable flow curves at lower $\dot{\epsilon}$ (<0.1 s⁻¹) and higher temperatures (> 1050 °C). The flow stress is found to decrease with increase in temperature or decrease in strain rates.
- (2) Based on analysis of processing map, Ni-25Cr-14W alloy has safe region for hot workability in the temperature range of 1000–1200 °C and strain rates of 0.001–0.1 s⁻¹ with maximum efficiency (η) of ~44% at 1175 °C and 0.001 s⁻¹.

- (3) Decrease in strain rates and increase in deformation temperature resulted in increase in recrystallization fraction, whereas higher strain rate ($>0.01 \text{ s}^{-1}$) and lower temperature ($<1150 \text{ }^\circ\text{C}$) have neckless structure.
- (4) The constitutive equation for flow stress as per Arrhenius model has been written as

$$\dot{\epsilon} = 2.172 \times$$

$$10^{16} [\sinh(0.00608\sigma)]^{4.53} \left[\exp\left(\frac{-472.13 \times 10^3}{RT}\right) \right]$$

$$\sigma = \frac{1}{0.00608} \ln \left\{ \left(\frac{Z}{2.172 \times 10^{16}} \right)^{\frac{1}{4.53}} + \left[\left(\frac{Z}{2.172 \times 10^{16}} \right)^{\frac{2}{4.53}} + 1 \right]^{\frac{1}{2}} \right\}$$

- (5) The multi-step forging, with varying temperature or strain rate during deformation, has not yielded complete recrystallization of microstructure, indicating delayed or early stage of DRX mechanisms.

Acknowledgments

The authors are grateful to Director, LPSC for granting permission to publish this work.

Author contributions

RRK contributed towards conceptualization, methodology, investigation, resources, formal Analysis, and writing—original draft. RKS contributed towards formal analysis, investigation, and writing—original draft. VF contributed towards methodology, investigation, formal analysis. NP contributed towards methodology, investigation, and formal analysis. CRA contributed towards resources and investigation. DT contributed towards resources and investigation. SVSNM contributed towards conceptualization, resources, supervision, formal analysis, and writing—review & editing.

Funding

This research did not receive any specific grant from funding agencies in the public, commercial, or not-for-profit sectors.

Data Availability

The raw/processed data required to reproduce these findings will be made available on reasonable request.

Declarations

Conflict of interest On behalf of all authors, the corresponding author states that there is no conflict of interest.

Supplementary Information

The online version contains supplementary material available at <https://doi.org/10.1557/s43578-024-01390-w>.

References

1. R.C. Reed, *The Superalloys Fundamentals and Applications*, 1st edn. (Cambridge University Press, Cambridge, 2006)
2. G. Lucacci, *Steels and Alloys for Turbine Blades in Ultra-Supercritical Power Plants* (Elsevier, Amsterdam, 2017)
3. K.L. Kruger, *HAYNES 282 Alloy* (Elsevier, Amsterdam, 2017)
4. A. Di Gianfrancesco: Alloy 263. *Mater. Ultra-Supercritical Adv. Ultra-Supercritical Power Plants* 571 (2017).
5. J.J. de Barbadillo, *INCONEL Alloy 740H* (Elsevier, Amsterdam, 2017)
6. A. Di Gianfrancesco, *New Japanese Materials for A-USC Power Plants* (Elsevier, Amsterdam, 2017)
7. S.E. Atabay, O. Sanchez-Mata, J.A. Muñiz-Lerma, M. Brochu, Microstructure and mechanical properties of difficult to weld Rene 77 superalloy produced by laser powder bed fusion. *Mater. Sci. Eng. A* **827**, 142053 (2021)
8. A.P. Mouritz, *Introduction to Aerospace Materials* (Elsevier, Amsterdam, 2012), pp.251–267
9. S. Wu, H.Y. Song, H.Z. Peng, P.D. Hodgson, H. Wang, X.H. Wu, Y.M. Zhu, M.C. Lam, A.J. Huang, A microstructure-based creep model for additively manufactured nickel-based superalloys. *Acta Mater.* **224**, 117528 (2022)
10. P.R. Gradl, C.S. Protz, Technology advancements for channel wall nozzle manufacturing in liquid rocket engines. *Acta Astronaut.* **174**, 148 (2020)
11. I. Waugh, E. Moore, A. Greig, J. Macfarlane, W. Dick-cleland, Additive Manufacture of Rocket Engine Combustion Chambers Using the ABD R -900AM Nickel Superalloy. *SP2020 Virtual Conf. 17–19 March* No. March, 1 (2021).
12. A.P. Mouritz, *Introduction to Aerospace Materials* (Elsevier, Amsterdam, 2012), pp.39–56
13. G. Xu, C. Wu, Z. Liu, Y. Wang, Z. Zhang, Y. Li, P. Hu, Effects of the solution treatment on microstructural evolution, mechanical properties, and fracture mechanism of nickel-based GH4099 superalloy. *J. Miner. Mater. Charact. Eng.* **09**(06), 566 (2021)
14. M. Aqeel, S.M. Shariff, J.P. Gautam, G. Padmanabham, Liquation cracking in Inconel 617 alloy by laser and laser-arc hybrid welding. *Mater. Manuf. Process.* **36**(8), 904 (2021)
15. T. Zengwu, L. Jinshan, H. Rui, L. Yi, B. Guanghai, Effects of solution heat treatment on carbide of Ni-Cr-W superalloy. *Rare Met. Mater. Eng.* **39**(7), 1157 (2010)
16. Y. Liu, R. Hu, J. Li, H. Kou, H. Li, H. Chang, H. Fu, Hot working characteristic of as-cast and homogenized Ni-Cr-W superalloy. *Mater. Sci. Eng. A* **508**(1–2), 141 (2009)

17. C.J. Boehlert, S.C. Longanbach, A comparison of the microstructure and creep behavior of cold rolled HAYNES®230 alloy™ and HAYNES®282 alloy™. *Mater. Sci. Eng. A* **528**(15), 4888 (2011)
18. R. Dong, J. Li, T. Zhang, R. Hu, H. Kou, Elements segregation and phase precipitation behavior at grain boundary in a Ni-Cr-W based superalloy. *Mater Charact* **122**, 189 (2016)
19. H. Alloys: Haynes ® 230 ® alloy. (n.d.).
20. Y. Guan, Y. Liu, Z. Ma, H. Li, H. Yu, Hot deformation behavior and recrystallization mechanism in an as-cast CoNi-based superalloy. *Met. Mater. Int.* **28**(6), 1488 (2022)
21. H. Zhou, H. Zhang, J. Liu, S. Qin, Y. Lv, Prediction of flow stresses for a typical nickel-based superalloy during hot deformation based on dynamic recrystallization kinetic equation. *Rare Met. Mater. Eng.* **47**(11), 3329 (2018)
22. O. Lypchanskyi, T. Śleboda, K. Zygula, A. Łukaszek-Solek, M. Wojtaszek, Evaluation of hot workability of nickel-based superalloy using activation energy map and processing maps. *Materials (Basel)* **13**(16), 3629 (2020)
23. J. Qu, X. Xie, Z. Bi, J. Du, M. Zhang, Hot deformation characteristics and dynamic recrystallization mechanism of GH4730 Ni-based superalloy. *J. Alloys Compd.* **785**, 918 (2019)
24. Y.V.R.K. Prasad, T. Seshacharyulu, Modelling of hot deformation for microstructural control. *Int. Mater. Rev.* **43**(6), 243 (1998)
25. A.K. Godasu, U. Prakash, S. Mula, Flow stress characteristics and microstructural evolution of cast superalloy 625 during hot deformation. *J. Alloys Compd.* **844**, 156200 (2020)
26. S.V.S. Narayana Murty, B. Nageswara Rao, Ziegler 's criterion on the instability regions in processing maps. *J. Mater. Sci. Lett.* **7**, 1203 (1998)
27. S.V.S. Narayana Murty, B. Nageswara Rao, B.P. Kashyap, Instability criteria for hot deformation of materials. *Int. Mater. Rev.* **45**(1), 15 (2000)
28. Y.C. Lin, F.Q. Nong, X.M. Chen, D.D. Chen, M.S. Chen, Microstructural evolution and constitutive models to predict hot deformation behaviors of a nickel-based superalloy. *Vacuum* **137**, 104 (2017)
29. H.J. McQueen, N.D. Ryan, Constitutive analysis in hot working. *Mater. Sci. Eng. A* **322**(1–2), 43–63 (2002)
30. S.Y. Lee, Y.L. Lu, P.K. Liaw, L.J. Chen, S.A. Thompson, J.W. Blust, P.F. Browning, A.K. Bhattacharya, J.M. Aurrecoechea, D.L. Klarstrom, Tensile-hold low-cycle-fatigue properties of solid-solution-strengthened superalloys at elevated temperatures. *Mater. Sci. Eng. A* **504**(1–2), 64 (2009)
31. H.J. Lee, H. Kim, D. Kim, C. Jang, Microstructure evolution of a Ni-Cr-W superalloy during long-term aging at high temperatures. *Mater Charact* **106**, 283 (2015)
32. N.T.B.N. Koundinya, A.K. Karnati, A. Sahadevan, S.V.S.N. Murty, R.S. Kottada, Assessment of the post-dynamic recrystallization effects on the overall dynamic recrystallization kinetics in a Ni-base superalloy. *J. Alloys Compd.* **930**, 167412 (2023)
33. N.T.B.N. Koundinya, K. Sr iBharadwaj, E. Nandha Kumar, S.V.S. Narayana Murty, R.S. Kottada, understanding the hot working behavior of a Ni-base superalloy XH 67 via processing map approach. *Mater. Perform. Charact.* **9**(2), 20190110 (2020)
34. H. Yuan, W.C. Liu, Effect of the δ phase on the hot deformation behavior of Inconel 718. *Mater. Sci. Eng. A* **408**(1–2), 281 (2005)
35. J. Zhang, C. Wu, Y. Peng, X. Xia, J. Li, J. Ding, C. Liu, X. Chen, J. Dong, Y. Liu, Hot compression deformation behavior and processing maps of ATI 718Plus superalloy. *J. Alloys Compd.* **835**, 155195 (2020)
36. Z. Jia, X. Sun, J. Ji, Y. Wang, B. Wei, L. Yu, Hot deformation behavior and dynamic recrystallization nucleation mechanisms of inconel 625 during hot compressive deformation. *Adv. Eng. Mater.* **23**(3), 2001048 (2021)
37. K. Tang, Z. Zhang, J. Tian, Y. Wu, F. Jiang, Hot deformation behavior and microstructural evolution of supersaturated Inconel 783 superalloy. *J. Alloys Compd.* **860**, 158541 (2021)
38. K. Hrutkay, D. Kaoumi, Tensile deformation behavior of a nickel based superalloy at different temperatures. *Mater. Sci. Eng. A* **599**, 196 (2014)
39. X. Zhuang, Y. Tan, L. Zhao, X. You, P. Li, C. Cui, Microsegregation of a new Ni-Co-based superalloy prepared through electron beam smelting and its homogenization treatment. *J. Mater. Res. Technol.* **9**(3), 5422 (2020)
40. B. Verlinden, J. Driver, I. Samajdar, R.D. Doherty, *Thermo-Mechanical Processing of Metallic Materials*, 1st edn. (Elsevier, Amsterdam, 2007)
41. A.N. Jinoop, V. Anil Kumar, C.P. Paul, R. Ranjan, K.S. Bindra, Hot deformation behavior of Hastelloy-X preforms built using directed energy deposition based laser additive manufacturing. *Mater. Lett.* **270**, 7737 (2020)
42. R.D. Doherty, D.A. Hughes, F.J. Humphreys, J.J. Jonas, D. Juul Jensen, M.E. Kassner, W.E. King, T.R. McNelley, H.J. McQueen, A.D. Rollett, Current issues in recrystallization: A review. *Mater. Sci. Eng. A* **238**(2), 219 (1997)
43. F.J. Humphreys, M. Hatherly, *Recrystallization and Related Annealing Phenomena*, 2nd edn. (Elsevier, Amsterdam, 2004)
44. S. Tabaie, D. Shahriari, C. Plouze, A. Devaux, J. Cormier, M. Jahazi, Hot ductility behavior of AD730™ nickel-base superalloy. *Mater. Sci. Eng. A* **766**, 138391 (2019)
45. C.R. Anoop, R.K. Singh, R.R. Kumar, J. Miyala, S.V.S.N. Murty, K.T. Tharian, Development and validation of processing maps for hot deformation of modified AISI 321 austenitic stainless steel. *Mater. Perform. Charact.* **9**(2), 150 (2020)
46. C.R. Anoop, R.K. Singh, R.R. Kumar, M. Jayalakshmi, S.V.S.N. Murty, K.T. Tharian, Hot deformation studies and optimization of hot working parameters in custom 465° martensitic precipitation hardenable stainless steel. *Mater. Perform. Charact.* **9**(2), 170 (2019)

47. H.J. McQueen, C.A.C. Imbert, Dynamic recrystallization: Plasticity enhancing structural development. *J. Alloys Compd.* **378**(1–2), 35 (2004)
48. Y. V. R. K. Prasad, K. P. Rao, and S. Sasidhara: *Hot Working Guide* (2015).
49. J. Miao, S. Sutton, A.A. Luo, Deformation microstructure and thermomechanical processing maps of homogenized AA2070 aluminum alloy. *Mater. Sci. Eng. A* **834**, 142619 (2022)
50. S. Raveendra, S. Mishra, H. Weiland, and I. Samajdar: in *Appl. Texture Anal.*, edited by A.D. Rollett (John Wiley & Sons, Inc., 2008), pp. 523–528.
51. N. Pai, A. Prakash, I. Samajdar, A. Patra, Study of grain boundary orientation gradients through combined experiments and strain gradient crystal plasticity modeling. *Int. J. Plast.* **156**, 103360 (2022)
52. K. Thool, A. Patra, D. Fullwood, K.V.M. Krishna, D. Srivastava, I. Samajdar, The role of crystallographic orientations on heterogeneous deformation in a zirconium alloy : A combined experimental and modeling study. *Int. J. Plast.* **133**, 102785 (2020)
53. H. Li, X. Zhuang, S. Lu, S. Antonov, L. Li, Q. Feng, Hot deformation behavior and flow stress modeling of a novel CoNi-based wrought superalloy. *J. Alloys Compd.* **894**, 162489 (2022)
54. R. Peng, B. Wang, C. Xu, Y. Li, X. Fan, The formation of the cross shear bands and its influence on dynamic recrystallization and mechanical properties under Turned-Reverse Rolling. *Mater. Today Commun.* **26**, 102078 (2021)
55. H.K. Zhang, H. Xiao, X.W. Fang, Q. Zhang, R.E. Logé, K. Huang, A critical assessment of experimental investigation of dynamic recrystallization of metallic materials. *Mater. Des.* **193**, 108873 (2020)
56. Y.C. Lin, X.Y. Wu, X.M. Chen, J. Chen, D.X. Wen, J.L. Zhang, L.T. Li, EBSD study of a hot deformed nickel-based superalloy. *J. Alloys Compd.* **640**, 101 (2015)
57. J.J. Jonas, X. Queleñec, L. Jiang, É. Martin, The Avrami kinetics of dynamic recrystallization. *Acta Mater.* **57**(9), 2748 (2009)
58. C.M. Sellars, W.J. McTegart, On the mechanism of hot deformation. *Acta Metall.* **14**(9), 1136 (1966)
59. G. Asala, J. Andersson, O.A. Ojo, Analysis and constitutive modelling of high strain rate deformation behaviour of wire-arc additive-manufactured ATI 718Plus superalloy. *Int. J. Adv. Manuf. Technol.* **103**(1–4), 1419 (2019)

Publisher's Note Springer Nature remains neutral with regard to jurisdictional claims in published maps and institutional affiliations.

Springer Nature or its licensor (e.g. a society or other partner) holds exclusive rights to this article under a publishing agreement with the author(s) or other rightsholder(s); author self-archiving of the accepted manuscript version of this article is solely governed by the terms of such publishing agreement and applicable law.